J. Fluid Mech. (1994), *vol.* 261, *pp.* 1–19

Chaotic transitions of convection rolls in a rapidly rotating annulus

By A. C. OR

Department of Atmospheric Sciences and Institute of Geophysics and Planetary Physics, University of California, Los Angeles, CA 90024, USA

(Received 4 January 1993 and in revised form 10 August 1993)

Drifting convection rolls in a rapidly rotating cylindrical annulus with conical endwalls exhibit different transitional modes to chaotic flows at different Prandtl numbers. Three transition sequences for Prandtl numbers 0.3, 1.0 and 7.0 are studied for a moderately large Coriolis parameter and a wavenumber near the critical value using an initial-value code. As the Rayleigh number increases, each transition sequence first leads to a vacillating flow, and then to an aperiodic flow, the route of which is Prandtl-number dependent. From the low Prandtl number to the high Prandtl number, the transitions take different routes of torus folding, period doubling, and mode-locking intermittency.

1. Introduction

Thermal convection in a rapidly rotating annulus with slightly conical endwalls has been a valid model for stellar and planetary atmospheres (Busse 1976, 1983). Since recent efforts in simulating the flow have produced new dynamical features in the system (Or & Busse 1987; Schnaubelt & Busse 1992), considerable interest is directed toward the higher transitions. This interest is also motivated by complex chaotic behaviour reported in systems ranging from small oscillators to three-dimensional flows of continuous systems (see Thompson & Stewart 1986). Or & Busse (1987) found that for thermal Rossby waves, bifurcation of the basic mode lead immediately to a narrow range of skewed states known as the 'mixed' mode. The term 'mixed' describes a modal interaction between the first and the second radial modes. The first is the stable basic state; the second is unstable. When the mixed mode is unstable, it is shortly followed by a quasi-periodic, of vacillating state. The term 'vacillation' describes the spatial–temporal fluctuations of the travelling waves. This term was originally used to describe baroclinic waves that exhibit similar behaviour (for baroclinic waves, see Ghil & Childress 1987). The quasi-periodic state is more efficient in transporting heat and prevails over a larger range of Rayleigh numbers. In Lin, Busse & Ghil (1989) a truncated model of two radial modes was used to investigate the transition sequences to chaos following the vacillating mode. Recently, Brummell & Hart (1992) also computed the transition sequence originally reported by Lin *et al.*, using a high-resolution code (with 256×256 modes). Compared with Or & Busse (1987), however, Brummell & Hart used a mean-flow boundary condition that is free-slip rather than periodic. The two-mode model of Lin *et al.* is overtruncated, and therefore contains no mean flow. Brummell & Hart reported a different bifurcation sequence from that of Lin *et al.* Recently, Schnaubelt & Busse (1992) have extended the results of the problem to rigid boundary conditions but retained the periodic mean-

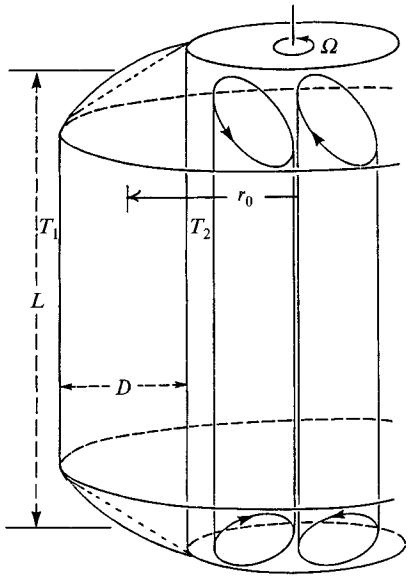

FIGURE 1. Geometry of the rotating annulus.

flow condition. Their results confirmed the period-doubling bifurcations originally found by Or & Busse (1987).

This paper focuses upon chaotic transitions following the vacillation mode in a moderately large system. With the integration scheme, sufficiently long time series are generated for analysing spatial and temporal behaviour. Since overtruncation of the spatial dependencies of variables can alter the physical nature of the flows (see discussions by Marcus 1981 and Curry *et al.* 1984) both spatial and temporal convergences of the simulated solutions are ensured. For a large system the computations effort can be enormous. Here we restrict the results to a fixed wavenumber close to the critical as well as three representative Prandtl numbers. This restriction is justified based on previous results that the bifurcation structure is quite insensitive to the wavenumber near its critical value. In §2, the mathematical formulation is developed. In §3, the mixed and the vacillating modes are reviewed briefly. In §4, the three transition sequences and their different chaotic routes are discussed. In §5, some concluding remarks are made.

2. Mathematical formulation

We consider a fluid layer in a thin-gap cylindrical annulus as shown in figure 1. The apparatus rotates about the cylinder's axis at angular speed Ω. The sidewalls are held at constant temperatures T_1 (inner wall) and T_2 (outer wall), with $T_2 > T_1$. Convection can occur in the form of rolls parallel to the spin axis if the temperature difference across the wall is sufficiently large. But unlike the ordinary rolls of Rayleigh–Bénard convection, the axial depth gradient of the layer presents a beta effect, which forces the rolls to drift as Rossby waves. With D^2/ν (ν is the kinematic viscosity) and $(T_2 - T_1)$ (Or & Busse 1987 used $(T_2 - T_1)P$) as the time and temperature scales, the vorticity and temperature equations according to the small-gap approximation are

$$\partial_t \Delta_2 \psi + J(\psi, \Delta_2 \psi) - 4\eta\, \partial_y \psi - \Delta_2^2 \psi + P^{-1} R\, \partial_y \theta = 0, \tag{1}$$

and

$$\partial_t \theta + J(\psi, \theta) + \partial_y \psi - P^{-1} \Delta_2 \theta = 0. \tag{2}$$

Both equations have nonlinear terms of the form $J(f,g)$, defined by

$$J(f,g) = \partial_y f \partial_x g - \partial_x f \partial_y g. \tag{3}$$

The Δ_2 denotes the two-dimensional Laplacian of the lateral coordinates x (radial) and y (azimuthal). The streamfunction, ψ, is defined by

$$\boldsymbol{v} = \boldsymbol{\nabla} \times \boldsymbol{k}\psi(x,y,t), \tag{4}$$

where $\boldsymbol{v}$ is the perturbation velocity field. The major parameters of the problem are defined as follows:

$$R = \frac{\gamma D^3 \Omega^2 r_0 (T_2 - T_1)}{\nu\kappa}, \quad \eta = \frac{\eta_0 \Omega D^3}{l\nu}, \quad P = \frac{\nu}{\kappa}, \tag{5}$$

where κ, ν, γ, r_0, l, and η_0 are respectively the thermal diffusivity, kinematic viscosity, coefficient of thermal expansion, mean radius, mean depth, and elevational angle of both endwalls. The system of equations (1), (2) is subjected to the conditions of no normal flow across sidewalls, isothermal walls, and periodic mean flow:

$$\psi = \theta = 0, \quad x = 0,1; \quad (\partial_{xx}^2 \bar{\psi})_{x=0} = (\partial_{xx}^2 \bar{\psi})_{x=1}. \tag{6}$$

Equations (1)–(3) are then approximated by an infinite set of ordinary equations using the Galerkin method, in which the expanding functions automatically satisfy boundary conditions. Solutions of the problem are sought in the following form:

$$\psi = \sum_{l,n}^{\infty} \sin(l\pi x)\,[\hat{a}_{ln}(t)\cos n\alpha(y-ct) + \check{a}_{ln}(t)\sin n\alpha(y-ct)] + \sum_{l=\text{odd}}^{\infty} \hat{a}_{l0}\, l\pi(x^2 - x) \tag{7}$$

and

$$\theta = \sum_{l,n}^{\infty} \sin(l\pi x)\,[\hat{b}_{ln}(t)\cos n\alpha(y-ct) + \check{b}_{ln}(t)\sin n\alpha(y-ct)]. \tag{8}$$

The second sum in ψ is to ensure a periodic mean flow (see Or & Busse 1987 and Schnaubelt & Busse 1992). The azimuthal mean flow depends only on x, and is given by

$$U(x) = -\overline{\partial_x \psi} = -\sum_{l=\text{odd}}^{\infty} \hat{a}_{l0}\, l\pi(2x-1) - \sum_{l=1}^{\infty} l\pi\, \hat{a}_{l0} \cos(l\pi x). \tag{9}$$

The mean flow at both walls is thus given by

$$U(0) = U(1) = -\sum_{l=\text{even}}^{\infty} l\pi \hat{a}_{l0}. \tag{10}$$

The mean thermal gradients at the walls are

$$(\overline{\partial_x T})_0 = \sum_{l=1}^{\infty} l\pi \hat{b}_{l0}, \quad (\overline{\partial_x T})_1 = \sum_{l=1}^{\infty} (-1)^l\, l\pi \hat{b}_{l0}. \tag{11}$$

When $\hat{b}_{l0}$ are time independent, the constant-flux condition gives

$$\sum_{l=\text{odd}}^{\infty} l\pi \hat{b}_{l0} = 0. \tag{12}$$

For a time-fluctuating mean field, local Nusselt numbers can be defined at each sidewall. Thus we have

$$Nu_0 = 1 + \sum_{l=1}^{\infty} l\pi \hat{b}_{l0}, \quad Nu_1 = 1 + \sum_{l=1}^{\infty} (-1)^l\, l\pi \hat{b}_{l0}. \tag{13}$$

Next, by inserting (7) and (8) into (1), (2), and averaging each resulting equation in turn by the set of weighting functions,

$$\sin(k\pi x)\cos m\alpha(y-ct), \quad \sin(k\pi(x)\sin m\alpha(y-ct), \tag{14}$$

we obtain an infinite set of nonlinear ordinary differential equations that govern the Fourier coefficients $\hat{a}_{ln}(t)$ and $\hat{b}_{ln}(t)$. According to our truncation scheme, modes are retained if their indices l,n satisfy

$$l+n \leqslant N_T.$$

The number of unknown coefficients at truncation parameter N_T is $2N_T^2$. The unknowns can be arranged as a state vector $\boldsymbol{x}$. The finite set can simply be denoted as

$$\boldsymbol{x} = \boldsymbol{f}(\boldsymbol{x}, R, \eta, P, \alpha), \tag{15}$$

which is then integrated forward in time by assigning an appropriate initial guess of the state. Solution sequences here typically run as functions of R for selected values of η, P and α.

With an explicit scheme, stability usually requires $\mathrm{d}t < \approx O(1/\max|\lambda|)$, where $\mathrm{d}t$ is the step size and $\max|\lambda|$ is the maximum eigenvalue of the linearized system. At $P = 1$, an explicit fourth-order Runge–Kutta scheme requires a step size of roughly 5×10^{-4} or smaller. A Rossby period of simulation then requires steps on the order of 10^2. At a smaller P, the number of steps is significantly larger owing to the much higher Rossby frequency. On the other hand, an implicit scheme requires larger storage and a matrix inversion per step (each step requires $216N_T^6$ arithmetic operations). But it is actually more promising for our problem, as its numerical stability permits a stretched step size by a factor of 10^2 over that of the explicit scheme. Typically, only 5–10 steps are needed to simulate one Rossby period. With the implicit scheme, the state vector at time $(n+1)\,\mathrm{d}t, \boldsymbol{x}^{n+1}$, and that at time $n\,\mathrm{d}t, \boldsymbol{x}^n$, are related by

$$\boldsymbol{x}^{n+1} = \boldsymbol{x}^n + a_1 \boldsymbol{r}_1 + a_2 \boldsymbol{r}_2, \quad \boldsymbol{r}_1 = \boldsymbol{f}(\boldsymbol{x}^{n+1})\,\mathrm{d}t, \quad \boldsymbol{r}_2 = \boldsymbol{f}(\boldsymbol{x}^{n+1} + q_1 \boldsymbol{r}_1). \tag{16}$$

For typical runs, we use a time step between 5×10^{-3} and 10^{-2} for $P > 1$ and one between 5×10^{-4} and 5×10^{-3} for $P = 0.3$. Overall, we ensure that step-size convengence is satisfactory by testing the accuracy of a sample of steady-state solutions against those obtained directly from the Newton–Raphson method. Spatial convergence is more difficult to achieve. It is ensured by comparing solutions of various N_T.

3. The regular solutions

We begin by reviewing some known solutions of the system. Several modes, up to the vacillation, have been studied in Or & Busse (1987) and Schnaubelt & Busse (1992). Only a brief account of these transitions will be provided here.

Our system preserves some symmetry of a layer: by reversing the body force and wall temperatures, the equations are unchanged. In the Fourier representation, this symmetry is characterized by the radial and azimuthal indice, l and n. Each linear mode and its Rossby frequency depend on a single pair of indices (l, n), classifiable according to whether $l+n$ is an even or odd integer. Since parity is preserved by the nonlinearity, depending on the parity of the sum of indices, the basic mode can be classified as even or odd. But here only the basic mode corresponding to the lowest indices (1, 1) is stable. All the higher even modes and all the odd modes are unstable. Also, rotation severely constrains the size of the rolls; the modal structure develops in the radial direction rather than in the azimuthal direction. The first odd mode thus corresponds to (2, 1) rather than to (1, 2). As R increases, the modes develop more complex spatial structures through bifurcations. Symmetries are naturally lost in modal interactions. The linear result indicates that the first two neutral curves are close to each other and indeed nonlinear analysis shows that these modes interact. But since these modes are travelling waves and possess distinct Rossby frequencies, two possibilities arise: either the

interacting modes lock up and produce a single frequency, or the interacting modes maintain their own drift rates. In the first case, the resulting mode remains a periodic travelling wave. In the latter case, the resulting mode becomes quasi-periodic, or vacillating. In Or & Busse (1987) and here the bifurcation always lead to the periodic 'mixed' mode. Only a subsequent transition of this mode gives rise to quasi-periodicity. In Schnaubelt & Busse (1992), the vacillation mode preceded the 'mixed' mode for $P = 7.0$. It is likely that such a difference is attributed to differences of boundary conditions. The modal interaction was discussed for the asymptotic limit, $\eta \to \infty$, by Busse (1986), who performed an explicit analysis.

The foregoing arguments are supported qualitatively by studying the onset Rayleigh numbers of the first two linear modes. For $P = 1.0$, these numbers are R_c ($R_c = 3.07 \times 10^4$) and $1.17R_c$. The bifurcation of the vacillation mode occurs at approximately $1.22R_c$. For $P = 0.3$, these numbers are again R_c ($R_c = 1.13 \times 10^4$) and $1.52R_c$. The bifurcation point occurs at about $1.54R_c$. In fact, the two frequencies of the quasi-periodic mode near the bifurcation point are reasonably close to those of the corresponding linear modes. According to linear theory, the ratio of the first mode's frequency to the second's frequency, c_2/c_1, is

$$\frac{c_2}{c_1} = \frac{\pi^2 + \alpha^2}{4\pi^2 + \alpha^2}. \tag{17}$$

At $\alpha \approx \alpha_c$, we have c_1/c_2 equal to 0.77 and 0.66 for $P = 1.0$ and $P = 0.3$ respectively. Based on the calculations near the bifurcation point, the ratios of the vacillation frequencies are 0.69 and 0.66, respectively, for $P = 1.0$ and $P = 0.3$. The correlation between the ratio of linear frequencies and that of the vacillating frequencies is even better at the lower Prandtl number, but is worse at the higher Prandtl number.

Certain qualitative features of the mixed and vacillating modes are of interest. Or & Busse (1987) noted that for the mixed mode, an increase of R leads to a decrease of Nusselt number or heat transport. The feature is not surprising in view of the skewed rolls, the strong mean shear, and the stronger phase shift between the hydrodynamic and thermal perturbational fields. After the unlocking of frequencies, the quasi-periodic mode is significantly more efficient in transporting heat. At each point at the walls, however, the heat flux is now fluctuating in time. The time-averaged heat fluxes into and out of the fluid are equal, but the fluctuation provides more freedom for optimizing the transport process. Schnaubelt & Busse remarked that the vacillation mode displays a certain relaxation response: a typical feature of the limit-cycle behaviour. A qualitative analogy with the Van der Pol's oscillator can be drawn, in that the odd mode in the vacillation plays the role of nonlinear damping. The presence of the odd mode tends to steepen the thermal boundary layer and thus enhances the heat transport, but also increases the diffusions in the flow field. Because the azimuthal interaction is weak and the radial interactions strong, the strongest coupling between the odd and the even modes is through the mean fields. Strong coupling between the (1, 1), (2, 1) and (1, 0) modes is evident from the solutions. The subtle balance between the odd and even modes obviously creates a limit-cycle response.

4. Transitions to chaotic solutions

As the Rayleigh number increases further, the vacillation becomes unstable. In Or & Busse (1987), Lin *et al.* (1989), Brummell & Hart (1992) and Schnaubelt & Busse (1992), the higher transition was studied only for the case of $\eta = 700$ and $P = 1.0$, and at a wavenumber equal to α_c. Both Or & Busse and Schnaubelt & Busse reported the

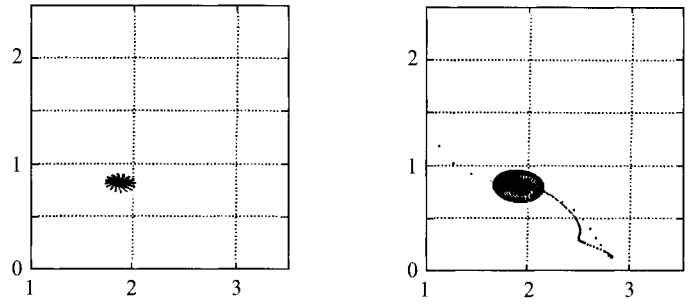

(*a*) $R=37\,600$

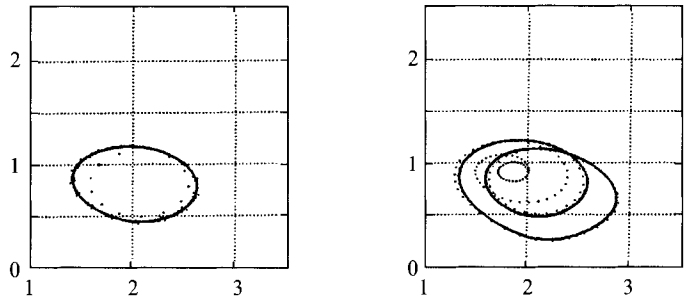

(*b*) $R=38\,500$

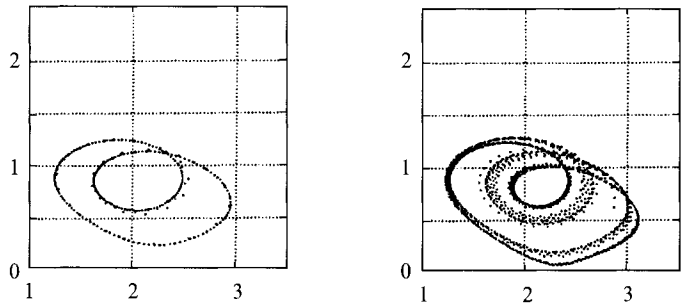

(*c*) $R=38\,800$

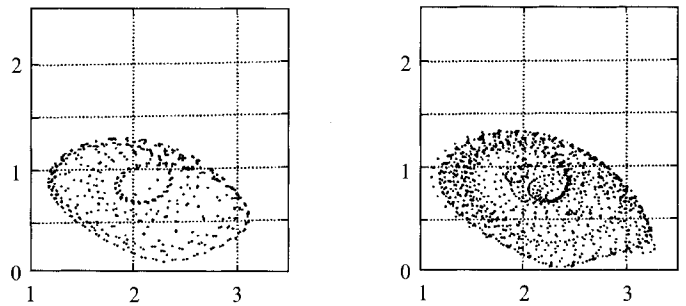

(*d*) $R=39\,000$

FIGURE 2. Phase portraits of a_{21} versus a_{11} for $P = 1.0$: a comparison between $N_T = 5$ (left column) and $N_T = 7$ (right column).

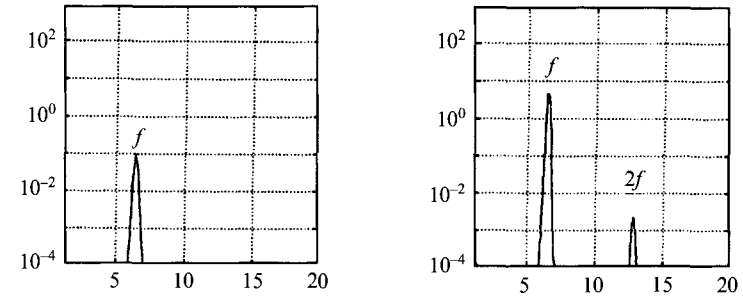

(*a*) $R=37\,600$

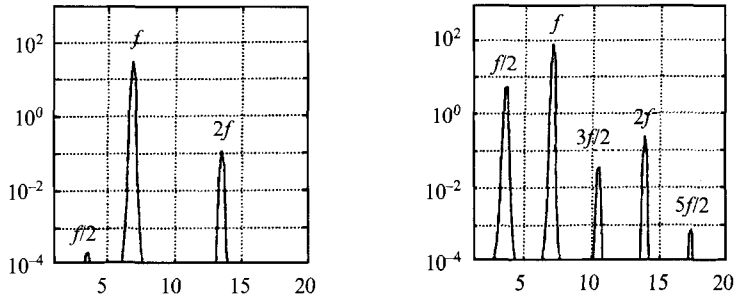

(*b*) $R=38\,500$

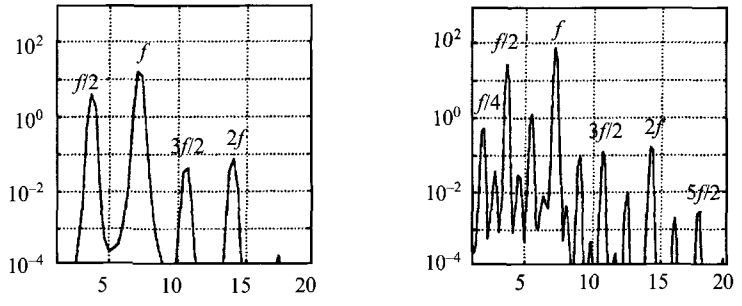

(*c*) $R=38\,800$

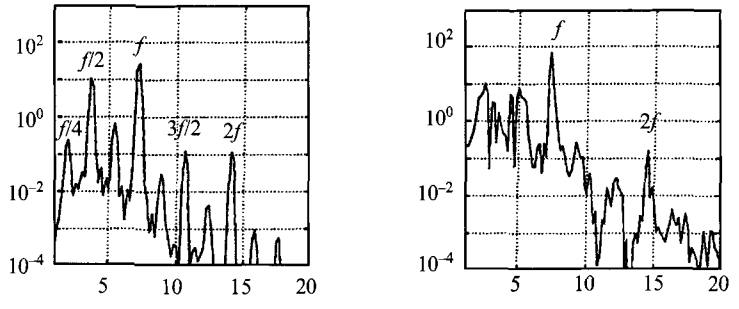

(*d*) $R=39\,000$

FIGURE 3. Power spectra of a_{11} corresponding to the panels of figure 2.

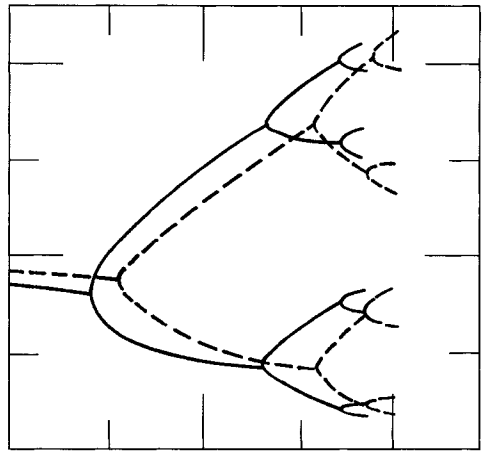

FIGURE 4. Bifurcation diagram for $P = 1.0$ showing up to the 8th period of the subharmonic sequence.

period-doubling bifurcations, which precede the chaotic flows. Brummell & Hart only found the first period-doubling bifurcation; the subsequent transition to chaos takes the route of a torus-winding instead. But since a different mean-flow boundary condition was used, the difference between the results of Brummell & Hart and Lin *et al.* does not reflect discrepancies. Apart from the results of Brummell & Hart, no detailed information has been published on the nature of the chaotic flow even for the well-studied case of $P = 1$, and $\eta = 700$ (except for the severely truncated model of Lin *et al.*). The case of $\eta = 700$ typically corresponds to the presence of a significantly strong Coriolis effect. A bifurcation sequence for a fixed wavenumber near its critical value should be quite adequate if the wavenumber is an insensitive parameter. To restrict the number of runs within the scope of our computational efforts, we explored three bifurcation sequences at representative Prandtl numbers: $P = 1.0$, 0.3 and 7.0. In the process, the differences in solutions due to the overtruncation effects are strong. Such differences obviously justify analysis of a large rather than small system.

4.1. *Prandtl number* = 1.0

The case of $\eta = 700$, and $\alpha = 9.4$ will be examined. Since considerable work has already been done on this case, our emphasis is to establish the spatial convergence of the solutions. The two-dimensional phase portraits of the major Fourier coefficients and their corresponding power spectra provide crucial information concerning the cascade. The four coefficients $\hat{a}_{11}$, $\hat{a}_{21}$, $\check{a}_{11}$, and $\check{a}_{21}$ provide important information about the bifurcation structures. The corresponding thermal coefficients show similar behaviour. In the portrait panels of figure 2, the horizontal and vertical axes represent $a_1 = (\hat{a}_{11}^2 + \check{a}_{11}^2)^{\frac{1}{2}}$ and $a_{21} = (\hat{a}_{11}^2 + \check{a}_{21}^2)^{\frac{1}{2}}$, respectively. In the left column, the panels correspond to $N_T = 5$ and in the right to $N_T = 7$. The step size of integration is between 0.005 and 0.01. The mixed mode appears as a point; the vacillating mode appears as a closed curve, or a limit cycle. Each subharmonic pitchfork bifurcation of the cascade doubles the number of windings of the existing loop. The similarity of the two sets of panels signifies spatial convergence. The corresponding power spectra are shown in figure 3. Only the spectra of a_{11} are shown, but those for a_{21}, a_{10} and Nu show similar information. The spectra of a_{11} do not have the Rossby frequency. Clearly both subharmonics and superharmonics are present. We are able to follow the amplitude

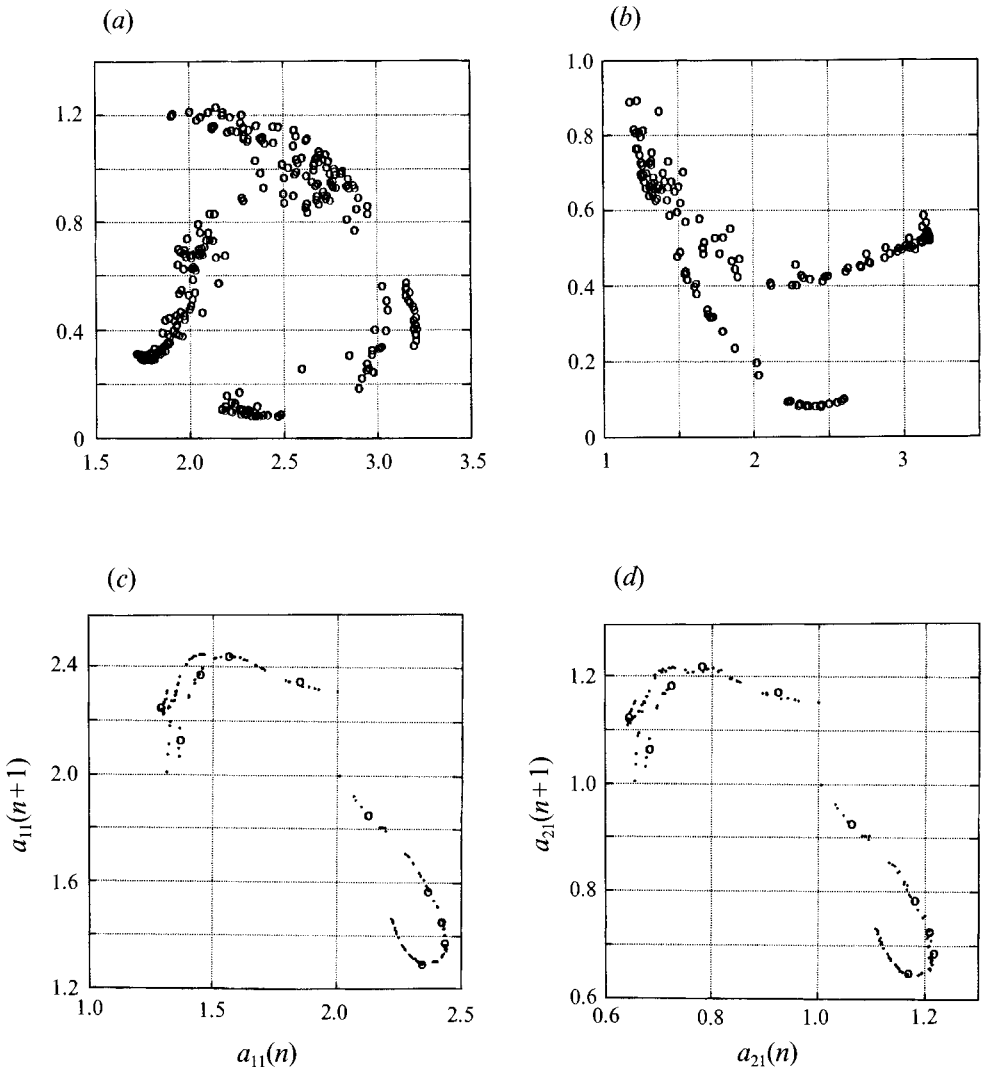

FIGURE 5. (*a*, *b*) Two-dimensional Poincaré maps showing different sections of the chaotic attractor in the (a_{21}, a_{11})-plane; (*c*, *d*) the shapes of the attractor via one-dimensional iterative maps.

versus Rayleigh number diagram up to the third subharmonic bifurcation in the cascade. Figure 4 clearly shows the 8-period cycle. Further transitions are beyond our graphic resolution. In the figure, the solid lines are for $N_T = 7$ and dashed lines for $N_T = 5$. The diagram shows that overtruncation delays the bifurcation. A well-established theory of the period-doubling cascade exists for one-dimensional maps (Feigenbaum 1984). The qualitative features of the transition here closely resemble the one-dimensional case, although the attractor here is clearly two-dimensional. Chaotic motions are found near the value of R corresponding to the accumulation point, 3.89×10^4, as predicted given the theoretical limiting value of 4.669 20... and the first few transition values found. Although most solutions were obtained at $N_T = 5$ and 7, we also computed the long-term chaotic behaviour for N_T as large as 11. Similar chaotic behaviour to that of $N_T = 7$ is found.

Next, we investigate the geometry of the attractor using the method of a Poincaré

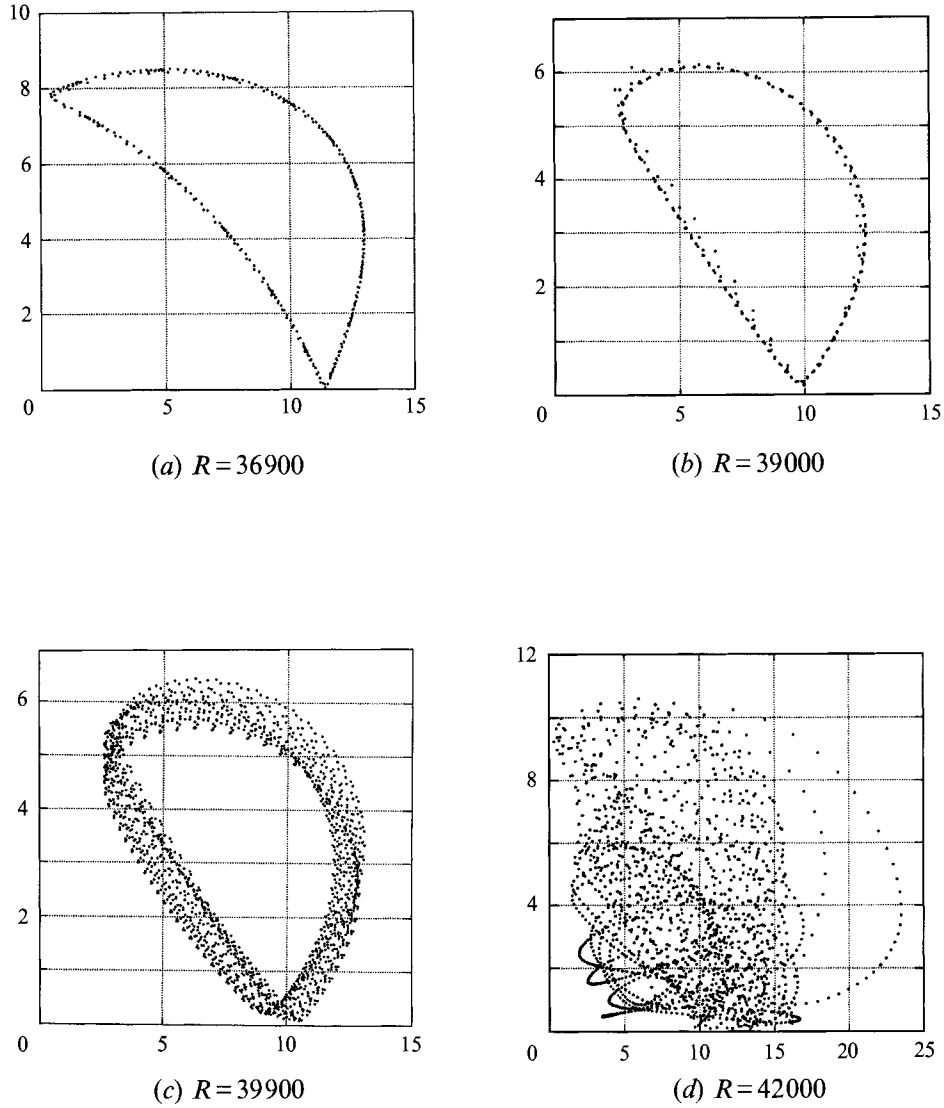

FIGURE 6. Phase portraits of a_{21} versus a_{11} for $P = 0.3$, showing the emergence of chaotic behaviour via quasi-periodicity.

map. A hypersurface in four-dimensional phase space is sought. Iterations on the set of points at which the trajectory of motion intersects the hypersurface provide the map; projection of this set of points onto a two-dimensional plane produces the shape of the attractor. Since we obtain the solutions by prescribing c at an arbitrary value, we can use a translation of time to eliminate the drift effect for the coefficient pairs $\hat{a}_{11}$ and $\check{a}_{11}$, and $\hat{a}_{21}$ and $\check{a}_{21}$. In this case, after the correction for translation, $\check{a}_{11}$ becomes very close to zero. There are two distinct maps that we can construct: (i) for $a_{11}/\hat{a}_{21}$ = constant, we plot a_{21} versus a_{11}; and (ii) for $a_{11}/\check{a}_{21}$ = constant, we plot a_{21} versus a_{11} (note: replacing the numerator of the ratio, a_{11} by a_{21}, will make no difference). For the case of $N_T = 9$ and $R = 39000$ and for the constant equal to 2π, the two maps are shown in figures 5(a) and 5(b), respectively. In figure 5(b), the lower of the two branches is present almost independent of the constant's value. The higher

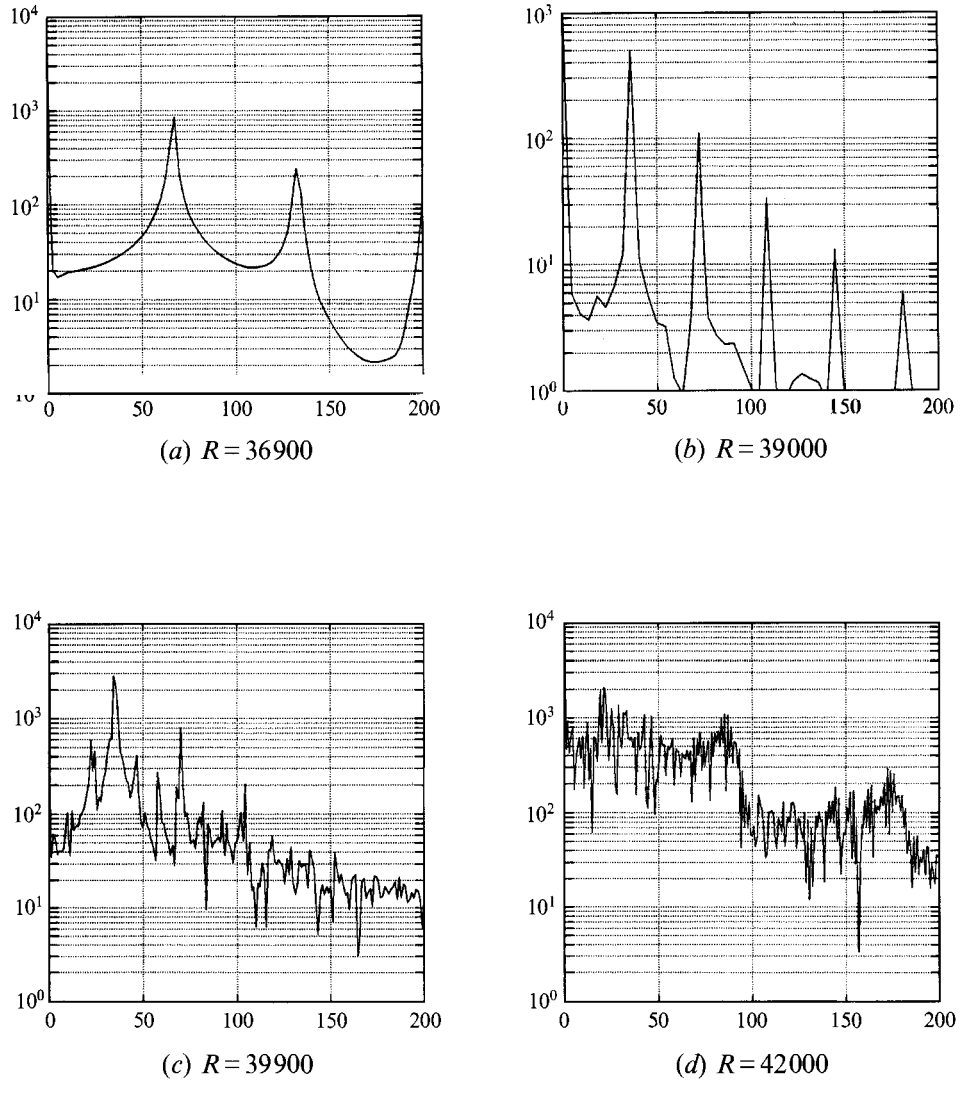

FIGURE 7. Power spectra of a_{11} corresponding to figure 6.

branch is not present when the constant is small. Poincaré maps of the same section as figure 5(*b*) have already been discussed in Lin *et al.* (1989). In their case, more branches occur in the stalk-and-leaves structure. Furthermore, they have a different orientation than ours. In figures 5(*c*) and 5(*d*), we also illustrate the iterative maps of $a_{11}(n+1)$ versus $a_{11}(n)$ and $a_{21}(n+1)$ versus $a_{21}(n)$ on the surface $a_{21}(n)/a_{11}(n) = 0.5$. These figures show the similarity of the two maps and the asymmetry of the attractor across the 45° diagonal line. The open circles correspond to a solution of $N_T = 11$.

4.2 *Prandtl number* = 0.3

This lower Prandtl number implies that hydrodynamic nonlinearity becomes more important than thermal nonlinearity. The vacillation mode is stable in a relatively wide range of R, from $1.54R_c$ to $3.51R_c$, where $R_c = 1.13 \times 10^4$. The Rossby frequency is also larger as the critical wavenumber becomes smaller, in this case, $\alpha_c = 6.9$. For the same

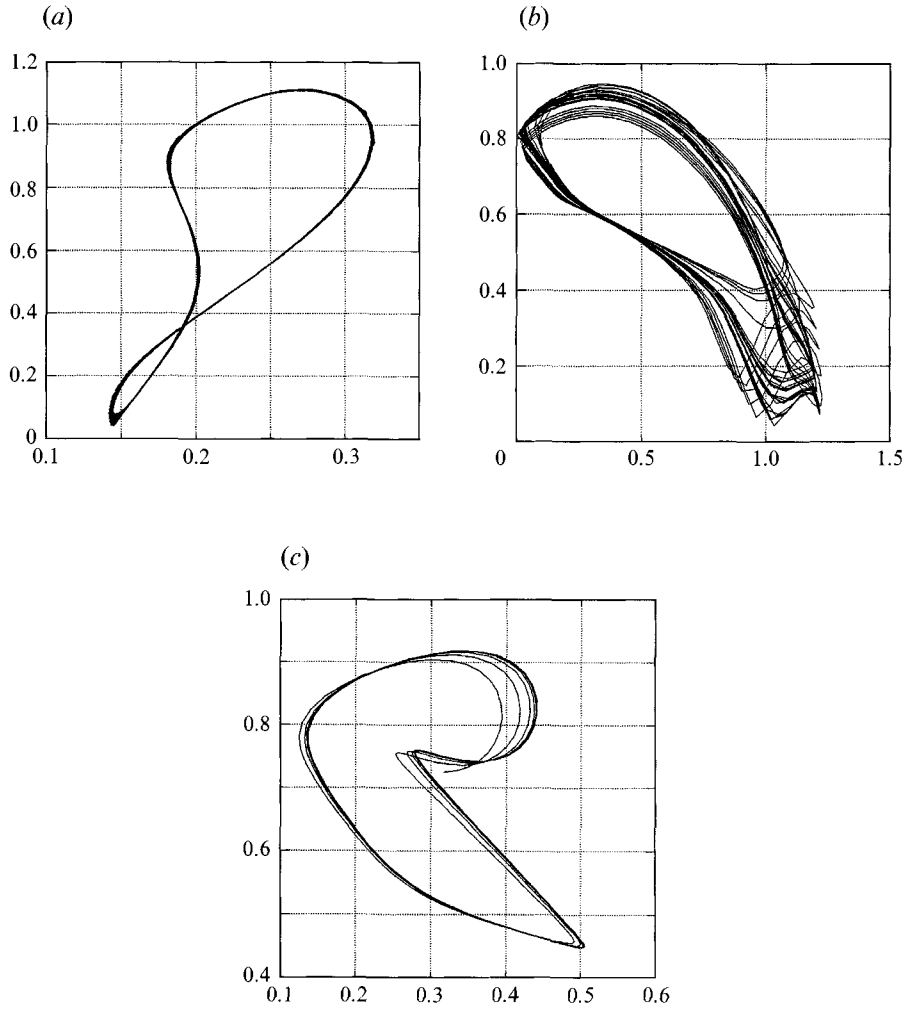

FIGURE 8. An example for $P = 7.0$ at $R = 122500$ showing the sensitivity of solutions to truncation. (*a*) $N_T = 5$, (*b*) $N_T = 7$, (*c*) $N_T = 9$.

η, the bifurcation sequence corresponds to $\alpha = 7.2$. The step size required for numerical stability is considerably smaller; in this case, it is between 0.0005 and 0.0025. The step size decreases as R gets higher. Unlike the case of $P = 1.0$, the lower N_T does not produce spatially converged results. At $N_T = 5$ and 7, we found phase-locking for vacillation at approximately $R = 4.9 \times 10^4$; following the locking, the limit cycle reverts back to steady state. At an even higher N_T, $N_T = 9$, the convergence improves significantly. At $R \approx 39000$, the limit cycle begins to display sideband modulation. The post-transient phase trajectory appears to fill up a thin 2-torus. Figure 6 contains the sequence of phase portraits to illustrate this change. The vacillation becomes aperiodic somewhere between $R = 39900$ and 42000. The power spectra shown in figure 7 are consistent with the indications of the phase portraits: first, a new but non-commensurate frequency appears as a small subharmonic peak in the panel for $R = 39000$. Then the broad-band spectrum follows, evident at $R = 42000$. The transitions shown in figures 6 and 7 have also been repeated for the case $N_T = 10$,

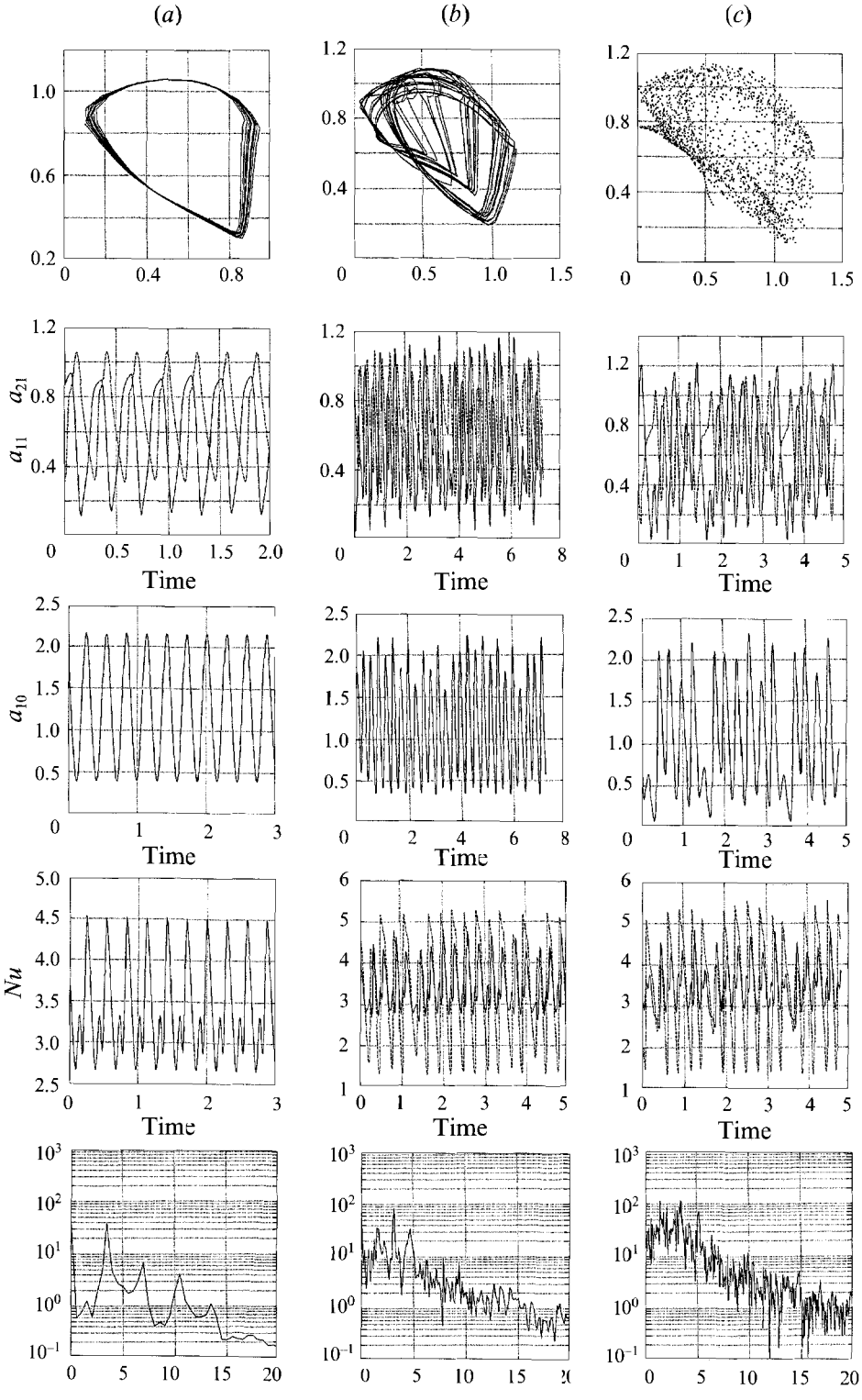

FIGURE 9. Phase portraits and time series showing the transition to an intermittency chaos at $P = 7.0$, and $N_T = 11$. (*a*) $R = 133000$; (*b*) $R = 13500$; (*c*) $R = 140000$.

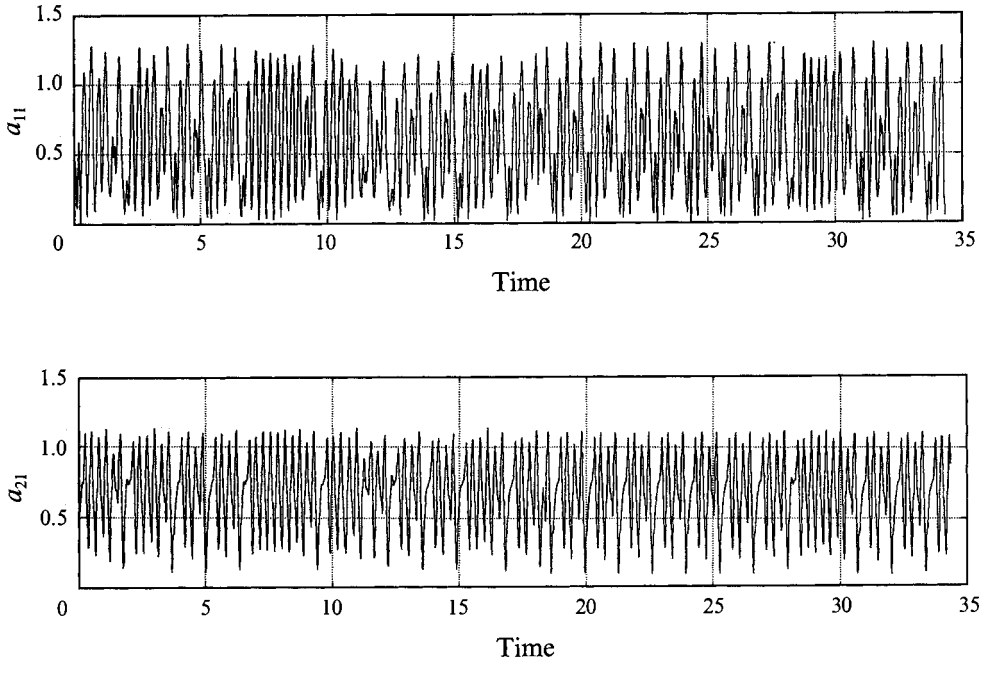

FIGURE 10. An extended time series in the chaotic region of $P = 7.0$ showing the intermittent behaviour.

showing similar results. Adding a third frequency to the solution turns out to be so drastic that it actually turns the regular behaviour chaotic. This remarkable but abrupt change is the subject of the classical paper by Newhouse, Ruelle & Takens (1978). They proved that a degree-n torus with $n \geqslant 3$ can be easily perturbed to strange attractors. Indeed, shortly after the third frequency emerges near $R = 39900$, we encounter a broad-band chaos. This transition pertains to a higher dimensional attractor. However, even without the Poincaré map, the transition is quite clearly illustrated by the phase portraits and power spectra.

4.3. *Prandtl number* = 7.0

We now turn to the case where thermal nonlinearity dominates hydrodynamic nonlinearity. This case can be realized in laboratory experiments using water as the fluid. Following the basic mode, we find the mixed mode only within a narrow range between $1.31R_c$ and $1.8R_c$ (where $R_c = 64000$). For R greater than $1.8R_c$, the mixed mode become unstable to vacillation following a Hopf bifurcation. For the higher Prandtl number, the vacillation mode is more sensitive to the truncation effect. Figure 8(*a–c*) provides an example of this effect. The panels indicate that the shape of the phase portrait for the same solution at $R = 122500$ and $\alpha = 11.5$ is completely distorted by changing N_T from 5 to 11. The panels for $N_T = 9$ and $N_T = 11$ (not shown) are almost the same, indicating convergence. As the subsequent flow field will show, flow is dominated by the odd modes, which require a higher spatial resolution to capture them. Having established spatial convergence at $N_T = 11$, we fix N_T at 11 and increase R further. Figure 9(*a–c*) consists of three columns of panels which represent (from left to right) solutions for $R = 133000$, 135800 and 140000. Running from top to bottom, the panels are respectively the phase portrait of a_{21} versus a_{11}, the time series of $\hat{a}_{11}$ (solid) and $\hat{a}_{21}$ (dashed), the time series of $\hat{a}_{10}$, the time series of

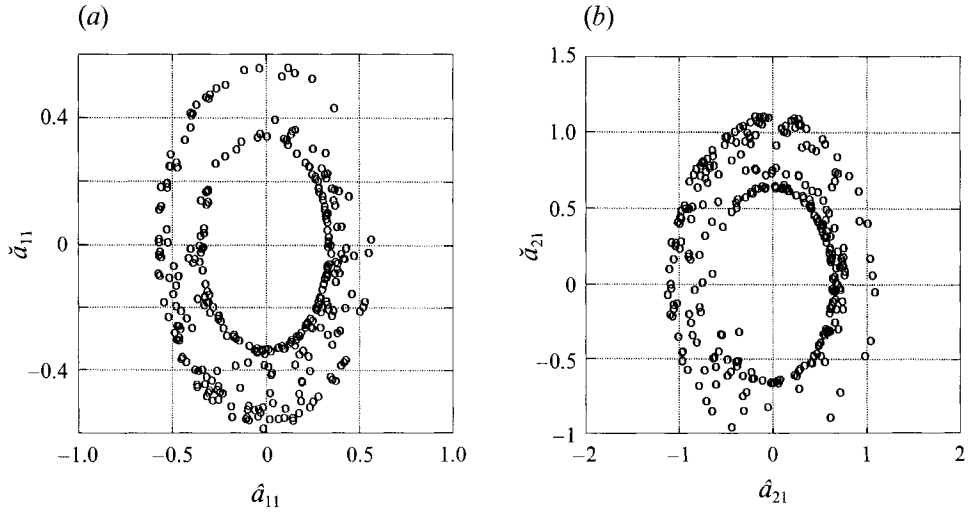

FIGURE 11. Poincaré sections of the chaotic attractor showing slow and fast parts of the loop.

Nu (Nu_0: solid; Nu_1: dashed), and finally, the power spectrum of the time series of a_{11}). These progressive panels clearly indicate that the limit cycle exhibits aperiodicity at $R = 140000$. Unlike the case of $P = 0.3$, the time series clearly suggests some mode-locking process. To further clarify the transition process, it is desirable to study long-term behaviour. At $R = 140000$, we obtain a run for 45 non-dimensional units of time, corresponding to 3320 points and at a step size of 0.01. Figure 10 shows that chaotic behaviour has the resemblance of mode-locking intermittency: the solution appears quite periodic for some time, but suddenly produces bursts of irregularity (at intermittent intervals). As for the period-doubling cascade, a fairly complete account of the process also exists for one-dimensional return maps (Pomeau & Manneville 1980). For the two-dimensional case, intermittent chaotic behaviour is best described by the 'drift ring' phenomenon (Ostlund *et al.* 1983). While the periodic solution appears as a stationary point in the Poincaré map, the chaotic solution is represented as a travelling point that rapidly drifts around the ring but spends most time near the stationary point. In figure 11, we construct similar Poincaré maps to illustrate this process, like those for $P = 1.0$. To get the right section, we set a_{11}/a_{21} equal to a constant instead. For this case, we let the constant be $\pi/6$. The drift-ring structure is evident from figure 11(*a*), showing $\check{a}_{11}$ versus $\hat{a}_{11}$, and from figure 11(*b*), showing $\check{a}_{21}$ versus $\hat{a}_{21}$. The points rotate counterclockwise. The drift-ring phenomenon exists in simple relaxation oscillators (see, for example, the Van de Pol problem, Thompson & Stewart 1986).

4.4. *A summary*

One reason for these varied transitions to chaos is that the problem contains multiple timescales. When the beta-plane effect is added, each of the two diffusive timescales is involved in the dynamical process even on the linear problem level. For low Prandtl number, the mean shear is strong but convection and heat transport are weak. The reverse is true for high Prandtl number. Thus, at low Prandtl number the vacillating mode persists to a considerably higher R with a strong mean flow where it turns weakly chaotic through the formation of a 3-torus. At high Prandtl number, convection is strong and is dominated by the odd modes, a double-roll rather than a single-roll pattern is found and the mean temperature profiles steepen near the wall to reflect a

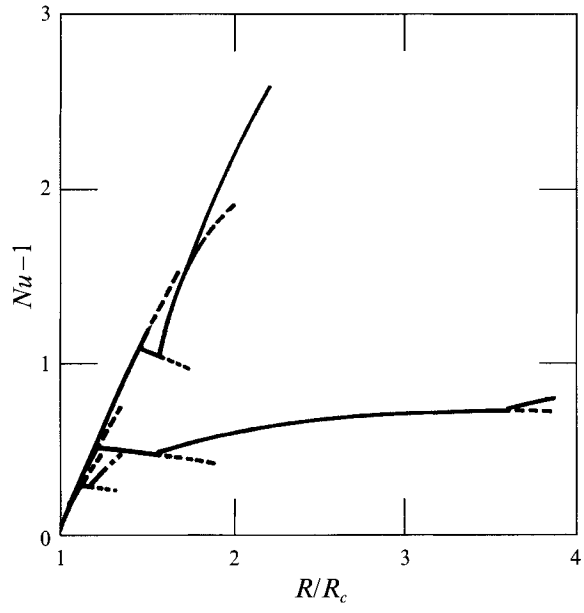

FIGURE 12. Mean Nusselt number versus Rayleigh number plots showing heat-transport dependency on Prandtl number.

P	R/R_c To even mode	To mixed mode	To vacillation	To higher transitions
0.3	1.0 ($R_c = 11253$)	1.17	1.54	Onset of quasi-periodic flow (2-torus) at 3.51
0.3	pitch-fork	pitch-fork	Hopf	Hopf Aperiodic flow with high regularity at 3.73
1.0	1.0 ($R_c = 30680$)	1.14	1.22	Period-doubling sequence from 1.24–1.26 (approx.)
	pitch-fork	pitch-fork	Hopf	Subharmonic pitch-fork Chaotic attractor of Feigenbaum type at 1.27
7.0	1.0 ($R_c = 63941$)	1.51	1.80	Onset of quasi-periodic flow (2-torus) at 2.05
	pitch-fork	pitch-fork	Hopf	Hopf Aperiodic flow resembled mode-locking intermittency at 2.18

TABLE 1. A summary of the transitional values of R

boundary-layer feature with high transport rate of heat. With a sufficiently large N_T, we found that flow following vacillation is grossly periodic but intermittently chaotic. Between the two Prandtl numbers, at $P = 1.0$, transition to chaos takes the period-doubling route. The major difference between the intermittency route and the Ruelle and Takens route to chaos is that the former goes from a quasi-periodic flow to a phase-locked periodic flow and then to chaos; while the latter goes from a quasi-periodic flow directly to chaos.

The existence of two means fields – those of the shear and temperature – and the coupling between the odd and even modes through these fields are especially complex.

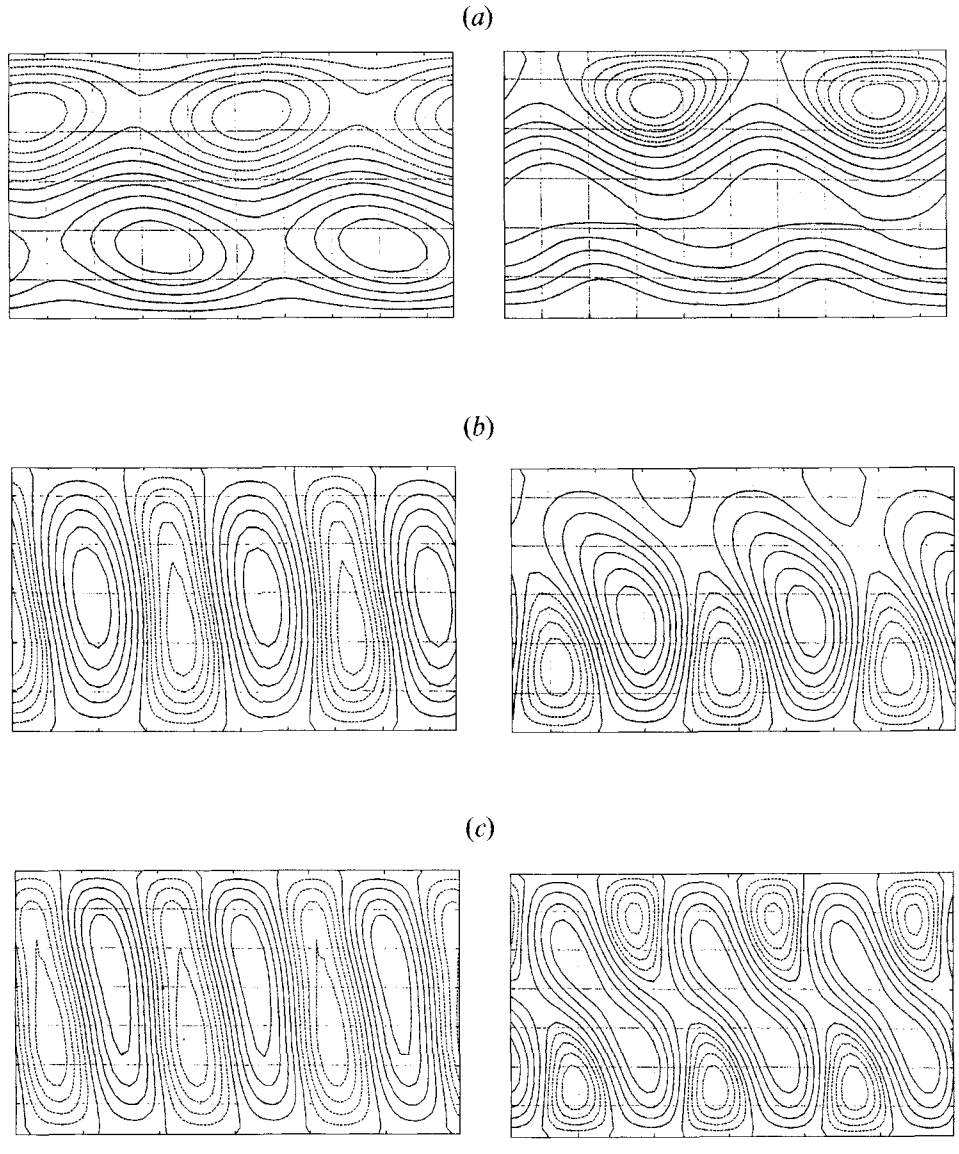

FIGURE 13. A comparison of contours of streamfunction among three Prandtl numbers in the chaotic region: two snapshots, low mean flow (left panels) and high mean flow (right panels). (*a*) $Pr = 0.3$, (*b*) $Pr = 1.0$, (*c*) $Pr = 7.0$.

The relative importance of these two fields obviously shapes the higher transitions following the quasi-periodic flow. The system is an example of a complex relaxation oscillator. Obviously, that relaxation process is strongly influenced by the ratio of the two diffusivities. Both the mean and fluctuating field boundary conditions are expected to influence the transitions significantly. The numerical results should be of considerable value for future work, especially in laboratory experiments. Table 1 compares the transition values of R and the types of transitions for the three Prandtl numbers. In figure 12, we summarize the heat transport rates by showing the mean Nusselt number, $0.5\,(Nu_0 + Nu_1) - 1$ versus R/R_c. The stable branches of solutions are shown as solid lines and the unstable branches as dashed. The diagram also shows how

Prandtl-number-dependent Nu is, even though the weakly nonlinear theory predicts that Nu is Prandtl-number independent. In figure 13, we compare the flow fields for (*a*) $Pr = 0.3$; (*b*) $Pr = 1.0$ and (*c*) $Pr = 7.0$. In each case, we plot ϕ, which includes the mean field. In each panel, the vertical axis represents the x-axis (pointed downward); the horizontal axis represents the axis $(y - ct)$. For each case, the left panel corresponds to a minimum in the mean flow coefficient $\hat{a}_{10}$, and the right panel corresponds to a maximum. In all cases the solutions are chaotic. We have $R = 39000$, 42000 and 140000 for cases (*a–c*), respectively. The flow fields obviously shift in shape throughout the chaotic cycle. The strongest mean shear appears in case (*a*); the steepest boundary-layer-type structure appears in case (*c*). In each case, the pattern exhibits a double-roll structure, at least during part of the cycle.

5. Concluding remarks

Although many studies of chaotic systems already exist, relatively few have been devoted to large systems. With the rapid growth of computing power, numerical simulations of real continuous systems are expected to gain importance. So far we have identified the different routes to chaotic behaviour for the different Prandtl numbers, for a pattern-forming flow the basic state of which is a travelling wave. The computational aspects are dramatically simplified given the two-dimensional nature of the flow. While detailed analysis of the bifurcation is beyond our scope, we have captured the major qualitative features of transitions to chaos.

Here we summarize the major results. At the low Prandtl number, the chaotic transition takes the route of torus folding. A third frequency emerges following the instability of the vacillation mode. This type of transition matches the description in the Newhouse–Ruelle–Takens (1978) scenario. At a Prandtl number of one, chaos is found following a period-doubling sequence. Here, we identified up to the third flip bifurcation. Chaotic behaviour occurs very close to the theoretical accumulation point, however, based on the first several transitional values in R and the theory of one-dimensional maps. At the larger Prandtl number, the results reflect mode-locking intermittency chaos. For specific purposes, two-dimensional Poincaré maps have been constructed to illustrate the shapes of the attractors.

Strong Prandtl-number dependence of the chaotic transitions is not surprising given the dramatic changes in heat transport and mean shear characteristics over the range of the ratio of diffusivities. When P is small, the mean shear is stronger and heat transport weaker. When P is large, the reverse becomes true. The change of the two mean quantities indicates shifts in dynamic balance. Schnaubelt & Busse noted that the vacillating mode, unlike the oscillatory modes of ordinary convection, actually enhances heat transport rather than decreases it; in fact, we found that heat transport is even stronger in chaotic flows. This property does not seem to be affected by the Prandtl number. The power spectra and flow patterns indicate that chaotic fluctuations are rather weak compared with the periodic coherent structures of vacillation. In fact, we found that the weak chaotic field persists for a much larger R (say, 1.5 times larger). Thus, in this example chaos does not lead to complete disorder; rather, it appears to optimize certain flow quantities such as heat transport and mean shear.

I am grateful to Professor M. Ghil of UCLA and the anonymous referees for suggestions and comments. This work was partly supported by the National Science Foundation under Grant number ATM90-13217.

REFERENCES

BRUMMELL, N. H. & HART, J. E. 1993 High Rayleigh Number β-convection. *Geophys. Astrophys. Fluid Dyn.* **68**, 85–114.

BUSSE, F. H. 1976 A simple model of convection in the Jovian atmosphere *Icarus* **20**, 255–260.

BUSSE, F. H. 1983 A model of mean zonal flow in the major planets. *Geophys. Astrophys. Fluid Dyn.* **23**, 153–174.

BUSSE, F. H. 1986 Asymptotic theory of convection in a rotating cylindrical annulus. *J. Fluid Mech.* **173**, 545–556.

CURRY, J. H., HERRING, J. R., LONCARIC, J. & ORSZAG, S. A. 1984 Order and disorder in two- and three-dimensional Bénard convection. *J. Fluid Mech.* **147**, 1–38.

FEIGENBAUM, M. J. 1984 Universal behavior in nonlinear systems. *Los Alamos Sci.* **1**, 4–27.

GHIL, M. & CHILDRESS, S. 1987 *Atmospheric Dynamics, Dynamo Theory, and Climate Dynamics.* Springer.

LIN, R. Q., BUSSE, F. H. & GHIL, M. 1989 Transition to two-dimensional turbulent convection in a rapidly rotating annulus. *Geophys. Astrophys. Fluid Dyn.* **45**, 131–157.

MARCUS, P. S. 1981 Effects of truncation in modal representations of thermal convection. *J. Fluid Mech.* **103**, 241–255.

NEWHOUSE, S. E., RUELLE, D. & TAKENS, F. 1978 Occurrence of strange axiom A attractors near quasiperiodic flows on $T^m, m \geqslant 3$. *Commun. Math. Phys.* **64**, 35–40.

OR, A. C. & BUSSE, F. H. 1987 Convection in a rotating cylindrical annulus. Part 2. Transition to asymmetric and vacillating flow. *J. Fluid Mech.* **174**, 313–326.

OSTLUND, S., RAND, D., SETHNA, J. & SIGGIA, E. 1983 Universal properties of the transition from quasi-periodicity to chaos in dissipative systems. *Physica* **8D**, 303–342.

POMEAU, Y. & MANNEVILLE, P. 1980 Intermittent transition to turbulence in dissipative dynamical systems. *Commun. Math. Phys.* **74**, 189–197.

SCHNAUBELT, M. & BUSSE, F. H. 1992 Convection in a rotating cylindrical annulus. Part 3. Vacillating and spatially modulated flows. *J. Fluid Mech.* **245**, 155–173.

THOMPSON, J. M. T. & STEWART, H. B. 1986 *Nonlinear Dynamics and Chaos*, pp. 264–272. John Wiley & Sons.